Asymmetric frequency multiplexing topological devices based on floating edge band

JIAJUN MA,[1] CHUNMEI OUYANG,[1,*] YUTING YANG,[2,*] DONGYANG WANG,[3,*] HONGYI LI, [1] LI NIU,[1] YI LIU,[1] QUAN XU,[1] YANFENG LI,[1] ZHEN TIAN,[1] JIAGUANG HAN,[1,4] WEILI ZHANG[5,*]

[1] Center for Terahertz Waves and College of Precision Instrument and Optoelectronics Engineering, and the Key Laboratory of Optoelectronics Information and Technology, Tianjin University, Tianjin 300072, People's Republic of China
[2] School of Materials Science and Physics, China University of Mining and Technology, Xuzhou 221116, People's Republic of China
[3] Optoelectronics Research Centre, University of Southampton, Southampton SO17 1BJ, United Kingdom.
[4] Guangxi Key Laboratory of Optoelectronic Information Processing, School of Optoelectronic Engineering, Guilin University of Electronic Technology, Guilin 541004, China
[5] School of Electrical and Computer Engineering, Oklahoma State University, Stillwater, Oklahoma 74078, USA
**Corresponding author: cmouyang@tju.edu.cn; yangyt@cumt.edu.cn; dongyang.wang@soton.ac.uk; weili.zhang@okstate.edu*

Received XX Month XXXX; revised XX Month, XXXX; accepted XX Month XXXX; posted XX Month XXXX (Doc. ID XXXXX); published XX Month XXXX

Topological photonics provide a platform for robust energy transport regardless of sharp corners and defects. Recently, the frequency multiplexing topological devices have attracted much attention due to the ability to separate optical signals by wavelength and hence the potential application in optical communication systems. The existing frequency multiplexing topological devices are generally based on the slow light effect. However, the resulting static spatial local mode or finely-tuned flat band has zero-group velocity, making it difficult for both experimental excitation and channel out-coupling. Here, we propose and experimentally demonstrate an alternative prototype of asymmetric frequency multiplexing devices including topological rainbow and frequency router based on floating topological edge mode (instead of localized ones), hence the multiple wavelength channels can be collectively excited with a point source and efficiently routed to separate output ports. The channel separation in our design is achieved by gradually tuning the bandgap truncation on a topological edge band over a wide range of frequencies. Wherein, a crucial feature lies in that the topological edge band is detached from bulk states and floating within the upper and lower photonic band gaps. More interestingly, due to the sandwiched morphology of the edge band, the top and bottom band gaps will each truncate into transport channels that support topological propagation towards opposite directions, and the asymmetrical transportation is first-time realized for the frequency multiplexing topological devices.

1. Introduction

Topological photonics[1-4] is an emergent field as the intersection of optical study and topological physics research, which has actively enlightened the wisdom on the novel control of electromagnetic (EM) waves. Optical waves engineered within a variety of topological phases[5-9] exhibit fascinating properties such as backscattering-immune and defect-insensitive, which are highly favored in scenarios demanding the reduction of crosstalk or scattering losses. For example, by employing an external magnetic field to gyrotropic materials, the quantum Hall effect can be imitated in photonic system to provide unidirectional propagation channel[10-14]. More convenient ways of achieving topological transport can be named as the photonic quantum spin Hall effect[15-19] or valley Hall effect[20-25] that require no time-reversal symmetry breaking. Following such recipes, topological photonics has served as a great support to the development of practical optical devices in the past few years[9, 26-29]. Within these available approaches, the valley topological photonic crystals (TPCs)[30-33] are particularly preferred for device application due to various aspects such as the easy design, robust topological transport, large bandgap, and compact size. A variety of novel devices have been proposed based on the valley TPCs, such as the reflectionless waveguides[34, 35], valley-conserved topological antenna[36], topological filters[37], topological cavities[38, 39], valley-dependent quantum photonic circuits [40], topological power splitters[41, 42], robust all-optical logic Gates[43], and topological lasers[44]. Note that these topological photonic devices based on valley TPCs suffer from propagation losses due to Anderson localization induced by fabrication disorder in the telecommunication wavelengths. However, at the lower frequencies (microwave and terahertz regime), Anderson localization is negligible as the length scale of such disorder is much smaller than the operating wavelength[45, 46].

On the other hand, frequency multiplexing devices[47-50] of rainbow trapping and frequency division are another family of essential components in optical communication systems that allow for a large capacity of information transmission. In traditional solutions with metamaterials[47, 51, 52], plasmonic waveguides[50, 53], nonlinear optics[54], or photonic crystals[55], the wave propagations are prone to defects, disorders, and bending losses. The idea of using topological materials, however, can provide a feasible plan to overcome these shortages, where novel photonic devices such as topological rainbows[56-60] and topological wavelength division multiplexers (WDMs)[61-64] have been presented. Among the existing demonstrations, the frequency channel isolation and division are usually induced by the topological slow light mode, where the wide range of wavevector components leads to spatial localization of topological edge mode. However, the resulting static spatial local mode or finely-tuned flat band is usually weak against perturbations or fabrication inaccuracies, and the localization size can hardly be ideal to avoid the coupling between different channels. Meanwhile, the excitation or out-coupling of edge modes in such topological frequency multiplexing devices is very difficult due to the zero group velocity of the slow light mode and flat edge band, which makes such frequency multiplexing topological devices unsuitable for practical use.

In this paper, we present an ideal solution to frequency multiplexing by proposing and experimentally demonstrating a new type of asymmetric propagating topological rainbow and frequency router based on floating topological edge mode. The multiple channels in the designed frequency multiplexing topological devices can be directly pumped by one single-point source placed at the end of the topological photonic crystal. These channels can then be easily coupled out to different ports. The principle of channel separation is accomplished by directly truncating the bandgap on a topological edge band, which is attributed to the novel feature of the floating edge band sandwiched by the top and bottom band gaps in our design. To be specific, through geometrical parameters tuning, it can be arranged that the frequency of the edge states in one TPCs slab corresponds to the band gap of the second TPCs slab, so that the wave propagation of this frequency channel finds prohibition at the interface between these two slabs. By successively implementing such design with gradually tuned TPC slabs, an edge band covering a wide range of frequencies can be truncated into multiple channels with each of them stopping at different spatial positions, and a propagating topological rainbow is thus designed. Meanwhile, proper domain walls are designed and attached to the prohibited positions of each frequency channel in the topological rainbow to design topological frequency router for coupling the energy out. More importantly, the upper and lower frequency gaps of the frequency multiplexing topological devices will each introduce truncation to provide different channels with opposite directions of propagation. The topological rainbow and frequency router are thus here first-time empowered with asymmetrical transportation.

2. RESULTS

2.1 METALLIC VALLEY TOPOLOGICAL PHOTONIC CRYSTALS AND FLOATING EDGE BAND

Here, we adopt the design of metallic valley TPCs[65] that consist of aluminum rods standing on a board in a triangular lattice, as depicted in Fig. 1a. Such TPCs support the propagation of spoof surface plasmon polaritons (SPP) due to the periodic structures[66]. The spoof SPP modes along the *z*-direction are self-confined. Compared to the traditional realization of two-dimensional systems that require a pair of parallel metallic plates for polarization selection and energy confinement[14, 16, 22, 67], the proposed design here does not need a covering lid and thus possesses an extra degree of freedom in tuning as the height of rods, which makes the metallic crystals better candidates for both implementing topological transport and device performance optimization.

A rhomboid unit cell with the lattice constant of a = 14 mm is shown in Fig. 1b (top panel), which consists of two metallic rods with a radius of r = 2.4 mm. When the sizes of the rods are the same, the photonic crystal possesses inversion symmetry, and the Dirac band dispersion emerges near the K (K') valley of the Brillouin zone and is shown in Fig. 1c as red dashed lines. A perturbation Δ can then be introduced into the size of sublattice rods to break the inversion symmetry. By implementing different height Δh or radius Δr to the rods in Fig. 1b (bottom panel), the degeneracy at the Dirac point is lifted and a complete photonic bandgap is formed at the K and K' valleys. By simultaneously tuning the height difference h_1-h_2 and the radius difference r_1-r_2 of metallic rods, a large bandgap of 21% (normalized to central frequency) is achieved in Fig. 1c.

By implementing a reversed set of parameters (height and radius) in the sublattice rods from the upper and lower regions in Fig. 1a, a domain wall can be formed as indicated with the dashed line. The mirror arrangement of rods across the domain wall constrains the valley Chern indices (in the lower two bands) as opposite for the two valley TPCs, where a contrasting integer valley Chern number ±1 is formed and is opposite for K and K' valleys. Topological edge modes are then formed and localized near the domain wall to provide topological transport.

On the contrary to traditional valley TPCs, it can be noticed in Fig. 1d that the edge mode bands in the metallic valley TPCs are detached from the bulk band projections and become floating in band gaps, which is an important feature that enables the design of frequency multiplexing topological devices such as topological rainbow and frequency router, and asymmetric transportation channels as will be discussed later. Note that different from the usual indication of band gaps as the full region between two bulk bands, we here use band gaps to specify the void region between the edge band and bulk bands. A little part of the edge mode is located above the air light line and can scatter into the background, thus only the spoof SPP edge modes outside the light cone are

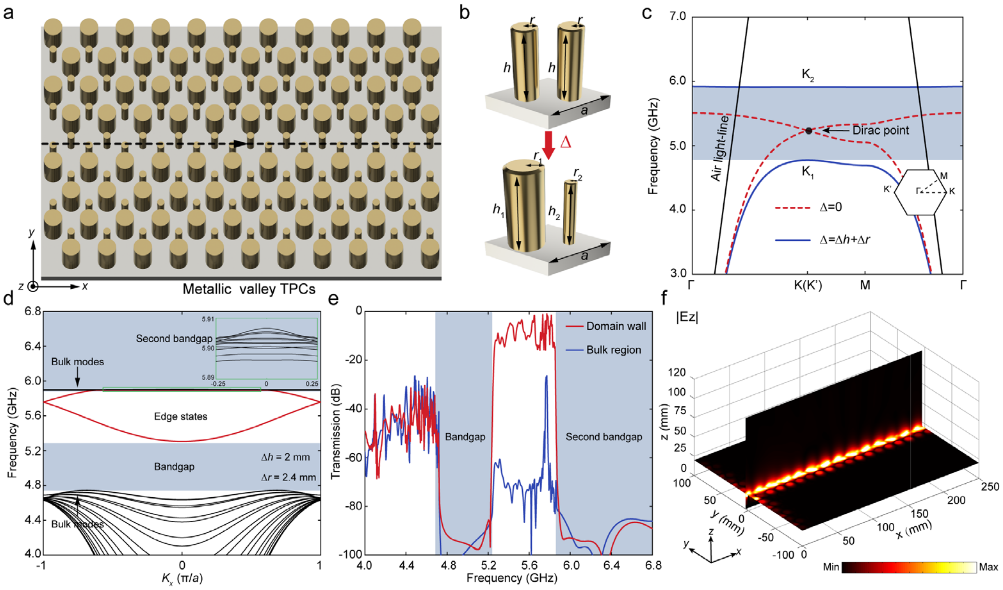

Fig. 1. Schematic of the broadband metallic valley TPCs. (a) Geometrical structure of the metallic valley TPCs, the domain wall is marked by black dashed lines. (b) The rhombic primitive cell consists of two equivalent/ nonequivalent metallic rods standing on a metallic plate. (c) Calculated band structures of the rhomboidal unit cell for the cases of Δ = 0 mm (red dash lines) and Δ = Δ*h* (2mm) + Δ*r* (2.4 mm) (blue solid lines). Black solid lines represent the dispersion of EM waves in the air (air light line), and the inset shows the first Brillouin zone. (d) Projected band dispersions of the ribbon-shaped supercell consisting of ten unit cells on each side of the domain wall. The red solid lines and black lines each indicate the edge states and projected bulk bands, respectively. The inset enlarges the area enclosed by the green rectangle around the upper bulk modes. (e) Simulated transmission for topologically protected edge states (red curve) and bulk states (blue curve) along the straight domain wall. (f) Simulated E_z field distribution of the topological edge states at 5.53 GHz.

used in our design. We then calculated the transmission spectra of these TPCs waveguides, as displayed in Fig. 1e, where apparently the edge modes provide broadband propagation along the domain wall in the valley TPCs. The simulated field pattern of the valley edge states at 5.53 GHz is also displayed in Fig. 1f, verifying that the edge modes are evanescently decayed along both the vertical(*z*) and transverse(±*y*) directions.

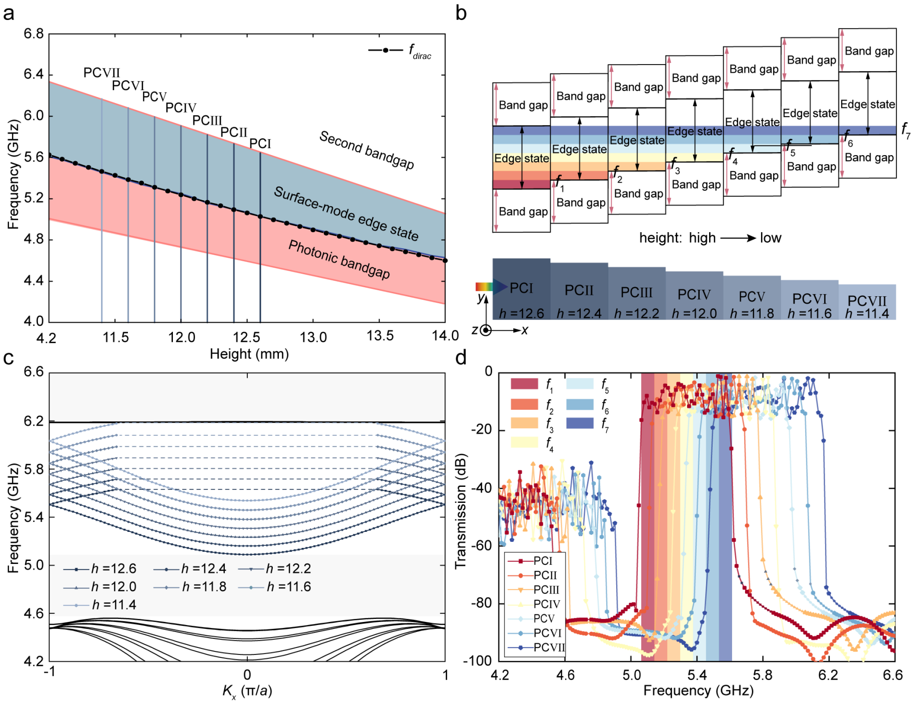

Fig. 2. Design of a seven-order topological rainbow. (a) Tuning the frequency range of edge states and photonic bandgap with the height of rods. The solid line denotes the relationship between the frequency *f* at the Dirac point and the rod height *h*. (b) Design of the topological rainbow with the excitation source put to the left side. (c) Surface band dispersions for the seven values of rod height *h* from 12.6 to 11.4 mm, calculated with ribbon-shaped supercells. (d) Transmission spectra of the seven metallic valley PCs with the rod heights *h* from 12.6 to 11.4 mm. The seven colored areas represent the different frequency ranges of surface waves corresponding to channels of f_1 to f_7.

2.2 ASYMMETRIC TOPOLOGICAL RAINBOW WITH POINT SOURCE EXCITATION

In this metallic valley TPCs, the freedom in the rod height can be utilized to manipulate the frequency of edge states and the band gaps. We first define an average rod height $h = (h_1 + h_2) / 2$, illustrated in Fig. 1b, for convenience. And as shown in Fig. 2a, while the average height is continuously tuned from h = 11 to 14 mm, the frequency range of the edge mode decreases from 5.61–6.34 GHz to 4.63–5.06 GHz (see Appendix A for more details), where we note that the higher bounds of the edge modes always merge with the upper bound of the first band gap as the flat bulk bands indicated with the dashed red line. Although there are only the lower bounds of edge state bands detached from bulk bands projection, it should be noticed that a second bandgap appears above the flat bulk band in Fig. 1d and Fig. 2a, and the flat bulk bands cover a very narrow frequency range so that the edge state bands can be effectively seen as being sandwiched by two bandgaps.

Taking advantage of the exotic feature of the floating topological edge band in the metallic valley TPCs, we proceed to design a broadband propagating topological rainbow by selecting a series of discrete parameters from Fig. 2a (see Appendix B for details). The proposed design of a seven-order topological rainbow is presented in Fig. 2b, where the edge mode frequency ranges (together with the band gap) are tuned as gradually increasing for each of the seven photonic crystals from left to right (noted as PCs, including PCI to PCVII). The frequency range of edge modes in each PCs are indicated by the arrowed line in black and the band gaps are indicated with red lines. It can be seen that there is a mismatch in the frequency range between two neighborhood PCs. Each of such differing frequency ranges are noted as f_1 to f_7 as shown in Fig. 2b, which serve as the multiplexing channels in the designed topological rainbow.

To understand the frequency channel separation, we first take the channel f_1 as an example. When the EM waves in the frequency range of f_1 is excited from the left side of PCI in Fig. 2b, the topological edge mode will propagate to the right coming across a band gap by reaching PCII (and no reflection due to topological protection), given the fact that the edge bands and band gaps in PCII are tuned to relative higher frequencies. This will lead to prohibited propagation of channel f_1 at PCII. Then if channel f_2 is excited from the left side of PCI in Fig. 2b, the propagation will be supported by both PCI and PCII, so the prohibited propagation will be at the interface between PCII and PCIII. Similarly, each channel of f_1 to f_7 will stop at different spatial positions of the TPCs, i.e., the interface between two adjacent PCs. This presents the desired frequency channel separation. Importantly, all the frequency channels can be easily excited with a single point source buried in the PCI at the domain wall, since the edge states in the PCI already cover the full frequency range from channel f_1 to f_7. We then realized the propagating topological rainbow with easy point source excitation. In Figs. 2c and 2d, we show the calculated band dispersion and transmission spectra for each of the seven PCs in the topological rainbow.

To experimentally verify the proposed seven-order topological rainbow, we fabricated a finite-sized sample consisting of 37 × 16 unit cells, where the number of unit cells in each block of PCs is 5 × 16, as shown in Fig. 3a. In the

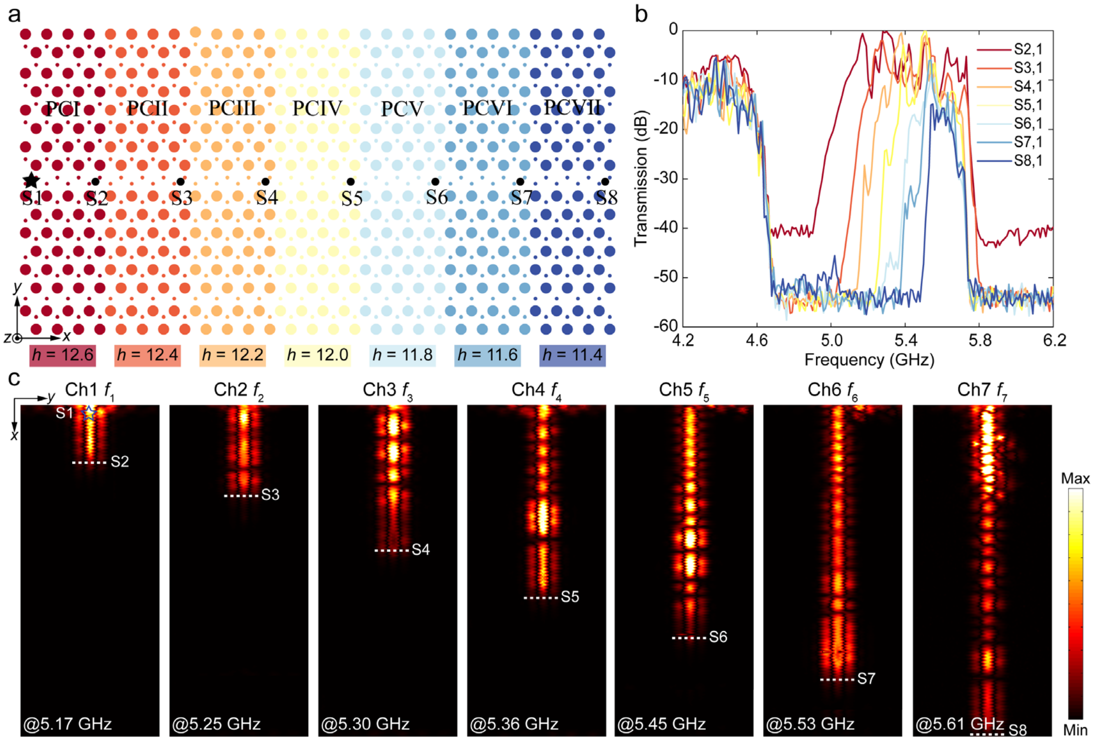

Fig. 3. Experimental characterization of the seven-order topological rainbow. (a) Schematic of the topological rainbow assembled from seven pieces of PCs. (b) Experimentally measured transmission spectra (in dB) of the topological rainbow when the source is placed at port S1. (c) Measured E_z field distributions of the edge states in the topological rainbow at 5.17, 5.25, 5.30, 5.36, 5.45, 5.53 and 5.61 GHz, respectively.

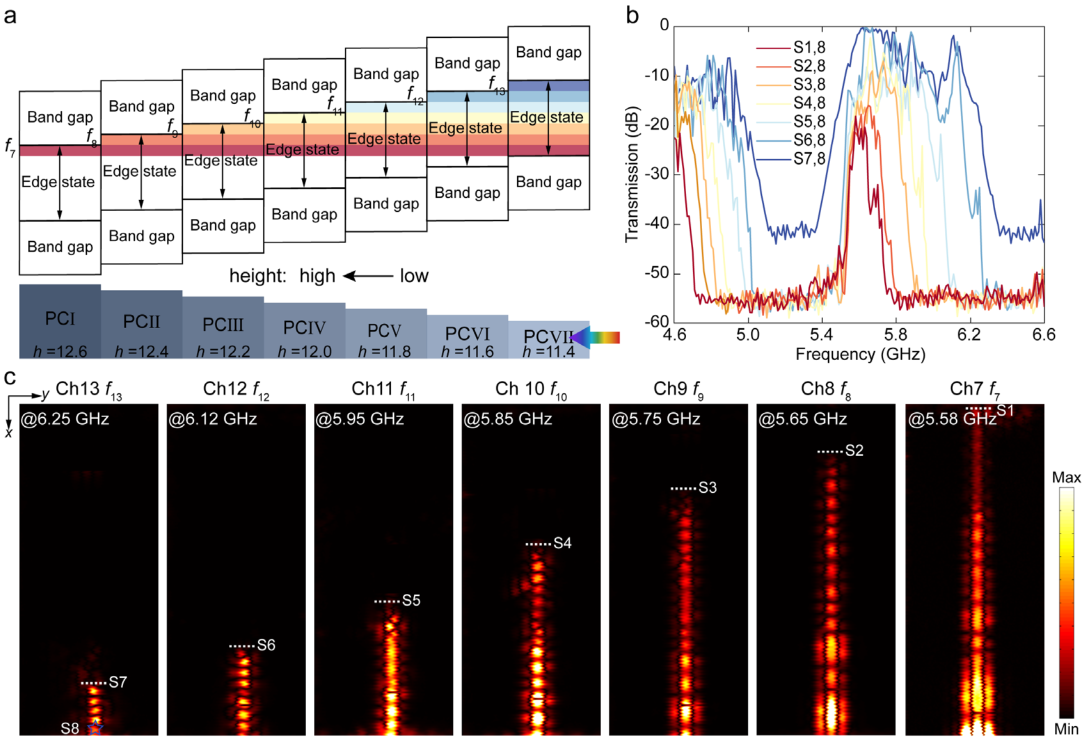

Fig. 4. Experimental characterization of the asymmetrical channels of the topological rainbow. (a) The channels of the topological rainbow when the excitation source is put to the PCVII on the right side. (b) Experimentally measured transmission spectra (in dB) of the topological rainbow when the source is placed at PCVII. (c) Measured E_z field distributions of the edge states in the topological rainbow at 5.17, 5.25, 5.30, 5.36, 5.45, 5.53 and 5.61 GHz, respectively.

experiment, a source antenna is put at the PCI and inserted through the drilled hole in a metallic substrate to excite EM waves, and the signals at different spatial positions are measured by a probe antenna. We experimentally measured the transmission spectra as shown in Fig. 3b, where the frequency ranges of edge states in different PCs of the topological rainbow are verified. By using microwave near-field scanning microscopy, we also directly mapped the electric field distributions along the domain walls and experimentally observed the prohibited propagation of EM waves for each rainbow frequency channel from f_1 to f_7 in Fig. 3c. It can be seen that the EM waves in each channel stop at distinct spatial positions, exhibiting the topological rainbow (see Appendix C for simulation results).

2.3 ASYMMETRIC TRANSMISSION CHANNELS OF THE TOPOLOGICAL RAINBOW

The seven-order topological rainbow can also be excited in a reversed way, where the source is put to the right-hand side of the TPCs, as shown in Fig. 4a. Interestingly, in such a configuration, the whole spectra of edge states in PCVII (instead of PCI) will be excited, and the mismatch between adjacent PCs (from right to left) due to the upper frequency band gap provides new channels of f_8 to f_{13} for topological transport as indicated with different colors in Fig. 4a. These channels also each find prohibited transmission at the interface between adjacent PCs, similar to the case in Fig. 2b. Such new channels support the transmission from right to left as opposite to the channels of f_1 to f_6, making the topological rainbow device asymmetric in transmission. It should be mentioned, however, the channel f_7 supports wave propagation in both directions.

We then experimentally characterized the topological transport with a point source placed in PCVII. The transmission spectra to different ports are shown in Fig. 4b, and the field distributions for several selected frequencies from channels f_7 to f_{13} are shown in Fig. 4c, where the rainbow effect is again demonstrated. The simulation results for the opposite channels are put in Appendix D.

The two types of excitation for the topological rainbow provide different working frequencies of 5.10–5.70 and 5.55–6.25 GHz, respectively, which originate from the different frequency ranges of edge states supported in PCI and PCVII. These asymmetric channels further increased the information-carrying capacities of the designed topological rainbow device, which can find application in novel optical communication systems.

2.4 ASYMMETRIC TOPOLOGICAL FREQUENCY ROUTER

To further enhance the results on asymmetric transportation and achieve the frequency division, we can assemble a design of asymmetric topological frequency router with multiple coupling ports so that the energy in each frequency channel can be coupled out instead of rainbow trapped. The design is

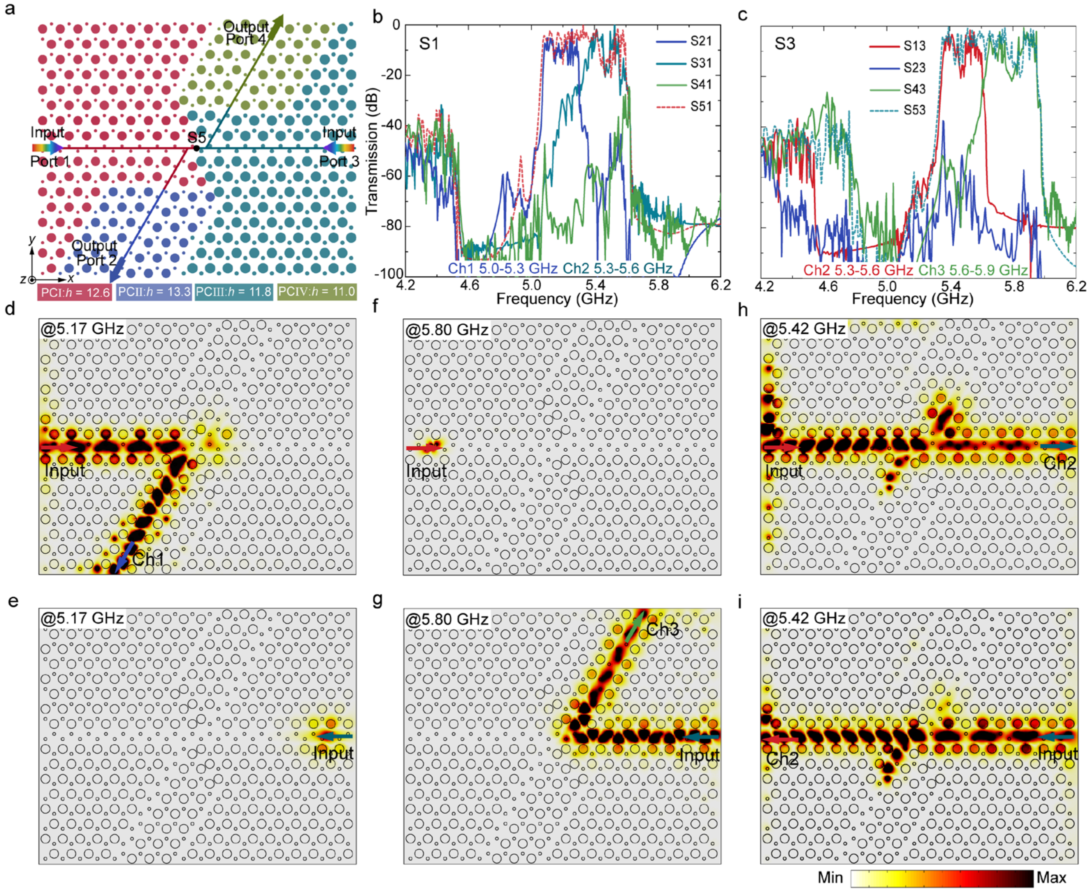

Fig. 5. Asymmetric propagating topological frequency router. (a) Schematic of the topological frequency division device that is composed of four TPCs designed with rods of different height *h*. Red, green, cyan and blue lines indicate the domain walls corresponding to the PCI, PCII, PCIII and PCIV, respectively. (b, c) Stimulated transmission spectra (dB) when the source is placed at Ports 1 and 3, respectively. The transmission spectra at Ports 1, 2, 3 and 4 are shown with the red, blue cyan and green lines. (d-i) Stimulated E_z field distributions at asymmetric frequency channels Ch1, Ch3 and Ch2, respectively.

shown in Fig. 5a, which consists of four metallic TPCs (PCI, PCII, PCIII and PCIV), and proper domain walls are designed and attached to the prohibited propagation positions of each frequency channel in the topological rainbow for coupling the energy out (see Appendix E for detailed parameters of TPCs and the design method of the asymmetric topological frequency router). The frequency multiplexing device consists of 18 × 18 unit cells, and four ports are designed with Ports 1 and 3 being the input ports and Ports 2 and 4 serving as output ports for different frequency channels.

The transmission spectra are shown in Figs. 5b-c for the configuration of the source being placed at ports 1 and 3, respectively. Three channels are designed to provide both asymmetrical and symmetrical transportation. From the field distributions in Figs. 5d-e, we can see that when a source antenna is put at the left side of Port 1 to excite all the frequencies of edge states in PCI, the frequency in Ch1 can propagate to Port 2, but such frequency channel is not supported while being excited from Port 3. On the other hand, when a source antenna is put at the right side of the device as Port 3 to excite the edge state in PCIII, as shown in Figs. 5f-g, the frequencies in Ch3 are supported and can propagate to Port 4, but this channel is not supported by exciting from Port 1. And a symmetrical transportation channel is also designed as the Ch2 in Figs. 5h-i that always exists regardless of the excitation source being located on the left or right.

Although the designed device supports asymmetric propagating channels, we should note that the propagation for each channel along the domain walls is reversible, e.g., from port 3 to port 1 for Ch2. We provide more discussion on this in Appendix F.

Due to the size limit of the permitted sample in the experimental setup and the requirement for the output ports to be on the same side, we choose to design and fabricate a dual-channel topological frequency router that consists of 19 × 15 unit cells shown in Fig. 6a. For experimental verification, we measured the transmission spectra from port 1 to port 2 and port 3 which are shown in Fig. 6b, where high transmittance for each of the two working channels can be found (simulations results are shown in Appendix G). It can be seen that a source antenna is put to port 1 to excite all the frequencies of the two channels. While being excited, the edge states of Ch1 and Ch2 will propagate along the domain wall of PCI to the first sharp bend. The Ch1 comes across with the forbidden propagation by PCIII and thus turns right entering PCII and subsequently arriving at port 2. The energy

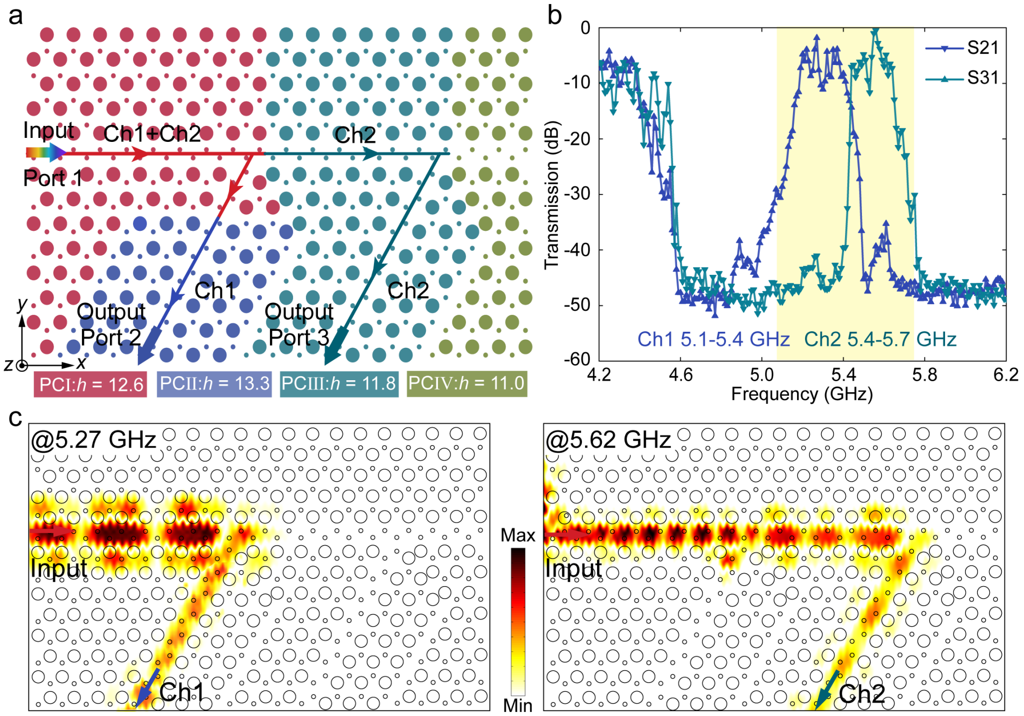

Figure 6. Dual-channel topological frequency router. (a) Schematic of the dual-channel topological frequency router that is composed of four TPCs designed with rods of different height *h*. Red, green, and blue lines indicate the domain walls corresponding to the PCI, PCII, and PCIII, respectively. (b) Experimentally measured transmission spectra (dB) at ports 2 and 3. The transmission spectra at Port 2 (S21) are shown with the blue line, while Port 3 (S31) is shown with the green line. Shadowed region represents the working frequency range. (c) Measured E_z field distributions at the two frequency channels that are coupled out through Ch1 and Ch2, respectively.

in frequency channel of Ch2, however, can keep propagating with PCIV, it is then coupled out from Port 3.Such sharp turns are possible due to the topological propagation of valley Hall edge states. It should also be noted that a part of energy in Ch2 can also make a turn towards Port 2, however, such propagations are stopped by PCII. As expected, the EMWs within 5.1–5.4 GHz propagate along the domain walls of PCII (Ch1) to output port 2, and those within 5.4–5.7 GHz transmit along the domain walls of PCIII (Ch2) to port 3. We also measured the field distributions along domain walls for each frequency channel, as shown in Fig. 6c, and it can be seen that the energy at different frequency channels is coupled out through separate ports. Note that the dual-channel topological frequency router can be composed of three metallic TPCs (PCI, PCII and PCIII), but we have added PCIV to block energy output on the right side of the router, so that the energy in the frequency channel Ch2 can make a sharp turn to port 3. Such results clearly demonstrated the idea of achieving frequency division with the proposed topological frequency router, which provides robust routes to realize multi-channel topological devices for optical communication.

3. METHODS

A. Numerical simulation

The band dispersion of the topological photonic crystals is numerically calculated with the frequency domain solver of commercial software COMSOL Multiphysics. The projected band diagrams are evaluated using a supercell configuration containing ten unit cells on either side of the domain wall, and periodic boundary conditions are imposed on the left and right sides. The simulations of the transmission spectra and electric field distributions are performed using the time domain solver of CST Microwave Studios. Open boundary conditions are applied in all directions, and the metals are set as perfect electric conductors.

B. Sample Fabrication

The TPC samples of the seven-order topological rainbow and dual-channel topological frequency division are fabricated with the traditional metal machining technique. They are composed of aluminum rods of different heights and radii placed on metallic substrates. The substrates are 10 mm thick and contain air holes in radius of 2 mm, and the aluminum rods are assembled to the metallic substrates through mechanical mounting. The fabricated samples are shown in Appendix H.

C. Experimental Characterization

A scanning near-field microwave system is employed to measure the transmission spectra and near-field electric field distributions. The system comprises a vector network analyzer (Keysight E5063A) and a 3D scanning stage. Two coaxial probes act as the emitting and probe antennas, respectively. The emitting antenna is placed in a drilled hole of the metallic substrate to excite the edge states and thus excites states with a full range of moments covering the -1 to 1 (π/a). However, the part within the light cone will scatter to surrounding air and does not contribute to the energy transport, and the other probe antenna is fixed to a module driven by a moving stage to measure the transmission data at discrete spatial positions. Detail setup can be seen in Appendix H.

5. CONCLUSION

In summary, we have proposed and experimentally realized the asymmetric propagating topological rainbow as well as a dual-channel asymmetric topological frequency router. The proposed topological multiplexing topological devices rely on robust topological propagating modes instead of localized modes and can capture and divide the EM signals into multiple frequency channels. These devices are designed based on metallic valley TPCs and spoof SPP modes, which are not only optimized with large bandgap, but can also be efficiently excited with a simple point source. By directly mapping the electric field propagation and measuring the transmission spectra, the spatial channel separation, asymmetric transportation, and out-coupling of different EM wave frequency channels have all been experimentally demonstrated. Our proposed asymmetric frequency multiplexing devices pave the way for designing robust and compact multi-frequency topological photonic devices. Moreover, such devices can be easily applied to terahertz or telecommunication wavelengths based on advanced micro-nanofabrication photolithography processes, providing a new method for the development of topological photonic devices for next-generation terahertz or optical communication.

APPENDIX A: THE PARAMETERS OF THE METALLIC VALLEY TPCS

We provide here the detailed geometrical tuning of edge states and band gap with the average height of the rods in the metallic valley TPCs, the data are presented in table S1.

Parameter (mm)	Bandgap (GHz)	Edge state (GHz)
$h = 11.0$	5.00 – 6.34	5.61 – 6.34
$h = 11.1$	4.98 – 6.30	5.58 – 6.30
$h = 11.2$	4.96 – 6.26	5.54 – 6.26
$h = 11.3$	4.93 – 6.21	5.50 – 6.21
$h = 11.4$	4.90 – 6.15	5.46 – 6.15
$h = 11.5$	4.86 – 6.10	5.42 – 6.10
$h = 11.6$	4.83 – 6.05	5.38 – 6.05
$h = 11.7$	4.81 – 6.00	5.34 – 6.00
$h = 11.8$	4.78 – 5.95	5.31 – 5.95
$h = 12.9$	4.75 – 5.91	5.28 – 5.91
$h = 12.0$	4.72 – 5.86	5.25 – 5.86
$h = 12.1$	4.68 – 5.81	5.21 – 5.81
$h = 12.2$	4.64 – 5.76	5.16 – 5.76
$h = 12.3$	4.61 – 5.72	5.13 – 5.72
$h = 12.4$	4.58 – 5.68	5.10 – 5.68
$h = 12.5$	4.55 – 5.64	5.07 – 5.64
$h = 12.6$	4.53 – 5.60	5.03 – 5.60
$h = 12.7$	4.50 – 5.56	5.00 – 5.56
$h = 12.8$	4.48 – 5.52	4.97 – 5.52
$h = 12.9$	4.46 – 5.48	4.94 – 5.48
$h = 13.0$	4.44 – 5.44	4.91 – 5.44
$h = 13.1$	4.42 – 5.40	4.88 – 5.40
$h = 13.2$	4.40 – 5.36	4.85 – 5.36
$h = 13.3$	4.37 – 5.32	4.82 – 5.32
$h = 13.4$	4.34 – 5.28	4.78 – 5.28
$h = 13.5$	4.31 – 5.24	4.75 – 5.24
$h = 13.6$	4.29 – 5.20	4.73 – 5.20
$h = 13.7$	4.26 – 5.17	4.71 – 5.17
$h = 13.8$	4.24 – 5.13	4.68 – 5.13
$h = 13.9$	4.21 – 5.09	4.65 – 5.09
$h = 14.0$	4.19 – 5.06	4.63 – 5.06

Table S1. Relationship between the working frequency f and the rod average height h when the perturbation Δ is the same (Δr = 2.4 mm and Δh = 2 mm). The rod radii are r_1 = 3.6 mm and r_2 = 1.2 mm, respectively.

APPENDIX B: THE PARAMETERS OF THE ASYMMETRIC TOPOLOGICAL RAINBOW

We provide here the adopted parameters for building the topological rainbow, the data are listed in Table S2.

Valley TPCs	Parameter (mm)	Bandgap (GHz)	Edge state (GHz)
PCI	$h = 12.6$	4.53 - 5.60	5.03 - 5.60
PCII	$h = 12.4$	4.58 - 5.68	5.10 - 5.68
PCIII	$h = 12.2$	4.64 - 5.76	5.16 - 5.76
PCIV	$h = 12.0$	4.72 - 5.86	5.25 - 5.86
PCV	$h = 11.8$	4.78 - 5.95	5.31 - 5.95
PCVI	$h = 11.6$	4.83 - 6.05	5.38 - 6.05

Table S2. Geometrical parameters are listed for the topological rainbow, which is composed of seven metallic valley TPCs noted as PCI to PCVII. The rod radii are r_1 = 3.6 mm and r_2 = 1.2 mm, respectively.

APPENDIX C: SIMULATION RESULTS OF THE TOPOLOGICAL RAINBOW

In this note, we present the simulation results for the topological rainbow where the propagation channels are from left to right. In Fig. S1a, we show the positions of ports on the sample. The transmission spectra from port S1 to S2-S8 are shown in Fig. S1b, where the high transmission through edge state frequencies can be seen. In Fig. S1c, the field distributions at different frequency channels are shown, and each channel stops at different spatial positions as confirmed by the experimental results in Fig. 3 of the main text.

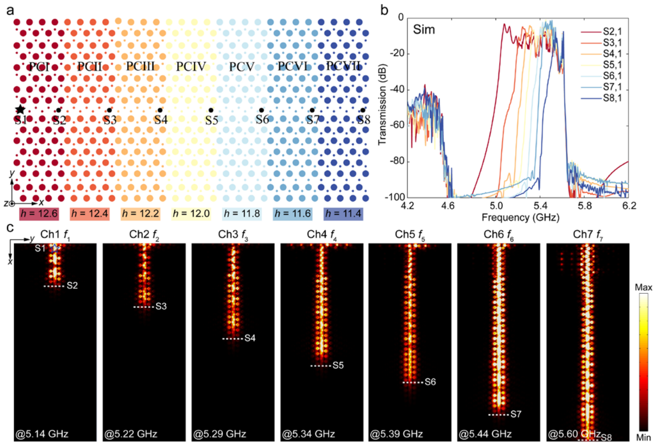

Fig. S1. Simulation results for topological rainbow. (a) Schematic of the piece-attached topological rainbow. (b) Simulated transmission spectra (in dB) when the source is placed at port S1, and the scattering parameters are shown for each port. (c) Simulated E_z field distributions of the edge states for each channel, and the prohibited propagation can be seen in the topological rainbow.

APPENDIX D: SIMULATION RESULTS FOR THE OPPOSITELY PROPAGATING CHANNELS OF THE TOPOLOGICAL RAINBOW.

The topological rainbow can also be excited in the opposite direction, and we provide the simulation results here. In Fig. S2a, we show the configurations in the simulation. The scattering parameters are calculated for the port as shown in Fig. S2b. We then show the propagation along the negative direction in Fig. S2c, where the energy in each frequency channel stops at different positions.

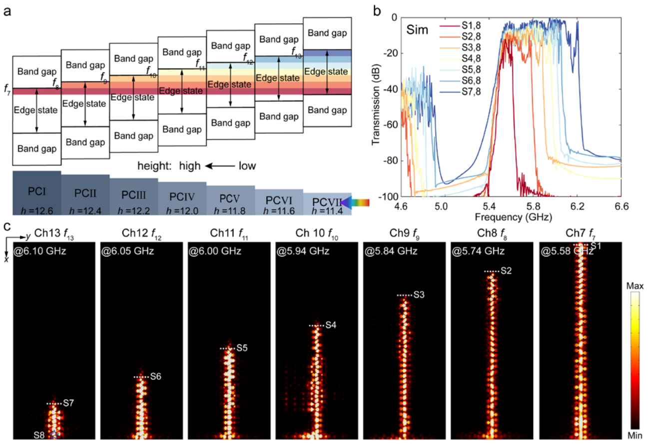

Fig. S2. Simulation results for the oppositely propagating channels of the topological rainbow. (a) Configuration for exciting opposite transmitting channels of the topological rainbow, where the point source is put to the right side. (b) Simulated transmission spectra (in dB) when the source is placed at port S8. (c) Simulated *Ez* field distributions of the edge states in each channel.

APPENDIX E: THE ADOPTED PARAMETERS AND DESIGN METHOD FOR THE ASYMMETRIC TOPOLOGICAL FREQUENCY ROUTER.

We show here the adopted parameters and design method for the asymmetric topological frequency router. The data are shown in Table S4. From the design method of the asymmetric topological frequency router in Fig. S3, we can see that when the source is located at different sides to excite the different edge states of TPCs, different functionalities of frequency division and rainbow trap can be achieved, respectively.

Valley TPCs	Parameter (mm)	Bandgap (GHz)	Edge state (GHz)
PCI	$h = 12.6$	4.53 - 5.60	5.03 - 5.60
PCII	$h = 13.3$	4.78- 5.95	5.31 - 5.95
PCIII	$h = 11.8$	4.37 - 5.32	4.82 - 5.32
PCIV	$h = 11.0$	5.00 - 6.34	5.61 - 6.34

Table S4. Geometrical parameters for the fabricated asymmetric topological frequency router, which is composed of four metallic valley TPCs as PCI to PCIV.

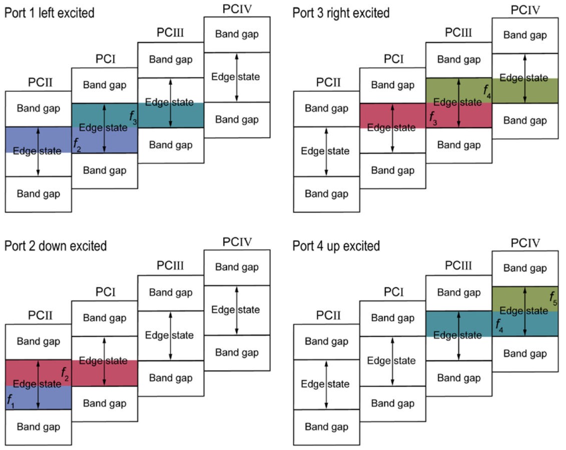

Fig. S3. The design of the asymmetric propagating topological frequency router with the excitation source put to different sides to excite the edge states of PCI to PCIV, respectively.

APPENDIX F: SIMULATION RESULTS OF ASYMMETRIC TOPOLOGICAL FREQUENCY ROUTER.

We here illustrate that although the designed router is asymmetric as a whole device, the propagation for each channel is reversible. We show the reversed excitation for different channels in Fig. S4, where the electric field distributions can be compared with that in Fig. 5.

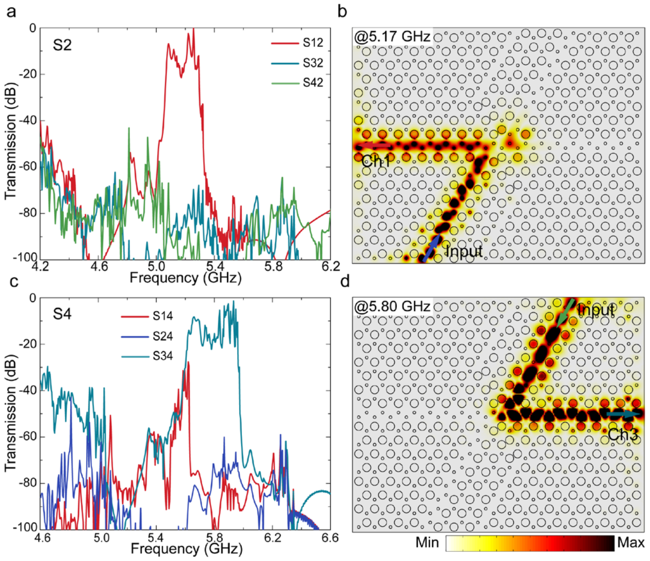

Fig. S4. Topological frequency router with the excitation source at the top and bottom sides. (a, c) Stimulated transmission spectra (dB) when the source is placed at Ports 2 and 4, respectively. The transmission spectra at Ports 1, 2, 3 and 4 are shown with the red, blue cyan and green lines. (b, d) Stimulated E_z field distributions at 5.17 and 5.80 GHz, respectively.

APPENDIX G: SIMULATION RESULTS OF THE DUAL-CHANNEL FREQUENCY ROUTER.

The simulation results for the dual-channel frequency router are displayed in Fig. S5a, the schematic of the simulation configuration is shown, and the calculated transmission from port 1 to port 2 and 3 are shown in Fig. S5b as blue and green curves, respectively. We then calculated the field distribution for selected frequencies from each channel in Fig. S5c, where the out-coupling for each channel is clearly shown.

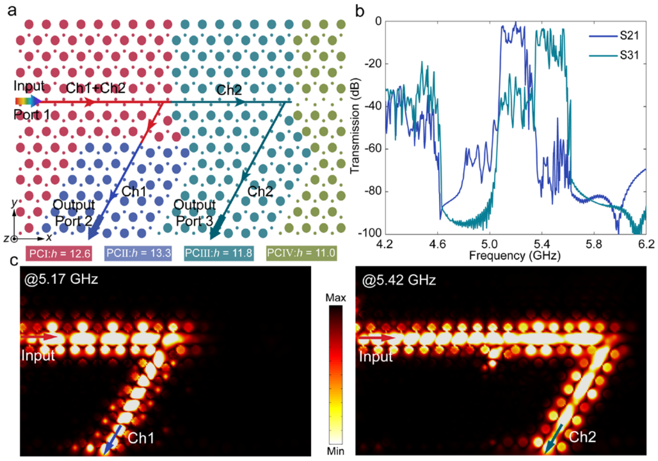

Fig. S5. Simulation results for dual-channel topological frequency router. (a) Schematic of the dual-channel topological frequency router that is composed of four metallic valley TPCs. Red, green, and blue lines indicate the domain walls corresponding to the PCI, PCII, and PCIII, respectively. (b) Stimulated transmission spectra (dB) from Port 1 to Ports 2 and 3. (c) Stimulated E_z field distributions for the two channels.

APPENDIX H: THE FABRICATED SAMPLE AND EXPERIMENTAL SETUP

The fabricated sample and experimental setup are shown in Figs. S6-S8.

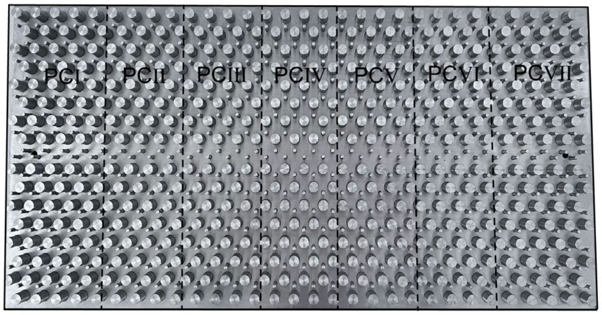

Fig. S6. Photograph of the seven-order topological rainbow assembled from seven pieces of metallic valley TPCs.

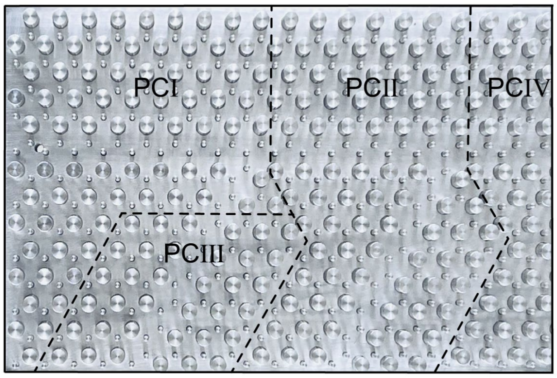

Fig.S7. Photograph of the dual-channel topological frequency router that is composed of four metallic valley TPCs designed with rods of different height *h*.

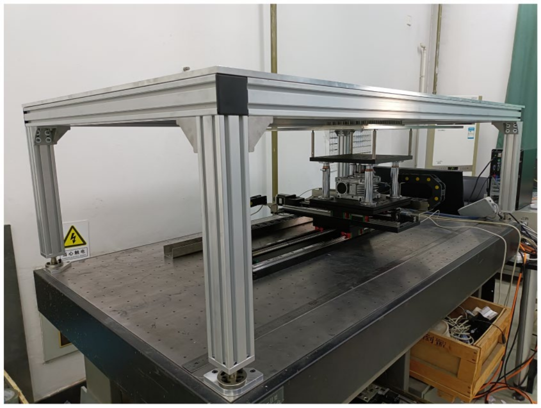

Fig. S8. Photograph of the measurement setup.

Funding. National Natural Science Foundation of China (Grant Nos. 62175180, 62027820, 62005193, 11874245, and 12004425), and the Natural Science Foundation of Jiangsu Province (Grant No. BK20200630). D. W. acknowledges support from the Anniversary fellowship of the University of Southampton.

Acknowledgments. J. M., D. W. and C. O. conceived the idea and designed the prototype. J. M. and L. N. performed the theoretical analysis and numerical simulations. J.M. and Y. Y. fabricated the sample and performed the experiments. C. O. led the project and J. M. wrote the manuscript. H. L., Y. L., Q. X., Y. L., L. N. and Y. Y. helped with the manuscript and data analysis, and J. H. and W. Z. supervised the project. All authors contributed to the manuscript.

Disclosures. The authors declare no conflicts of interest.

Data availability. Research data are not shared. The data that support the findings of this study are available from the corresponding authors upon reasonable request.

References

1. L. Lu, J. D. Joannopoulos, and M. Soljačić, "Topological photonics," Nat. Photonics **8**, 821-829 (2014).
2. T. Ozawa, H. M. Price, A. Amo, N. Goldman, M. Hafezi, L. Lu, M. C. Rechtsman, D. Schuster, J. Simon, and O. Zilberberg, "Topological photonics," Rev. Mod. Phys. **91**, 015006 (2019).
3. D. Smirnova, D. Leykam, Y. Chong, and Y. Kivshar, "Nonlinear topological photonics," Applied Physics Reviews **7**(2020).
4. S. Ma, B. Yang, and S. Zhang, "Topological photonics in metamaterials," Photonics Insights **1**, R02 (2022).
5. A. B. Khanikaev, S. H. Mousavi, W. K. Tse, M. Kargarian, A. H. MacDonald, and G. Shvets, "Photonic topological insulators," Nat. Mater. **12**, 233-239 (2013).
6. M. C. Rechtsman, J. M. Zeuner, Y. Plotnik, Y. Lumer, D. Podolsky, F. Dreisow, S. Nolte, M. Segev, and A. Szameit, "Photonic Floquet topological insulators," Nature **496**, 196-200 (2013).
7. D. Wang, B. Yang, W. Gao, H. Jia, Q. Yang, X. Chen, M. Wei, C. Liu, M. Navarro-Cía, J. Han, W. Zhang, and S. Zhang, "Photonic Weyl points due to broken time-reversal symmetry in magnetized semiconductor," Nat. Phys. **15**, 1150-1155 (2019).
8. M. Kim, Z. Jacob, and J. Rho, "Recent advances in 2D, 3D and higher-order topological photonics," Light: Science & Applications **9**, 130 (2020).
9. G. J. Tang, X. T. He, F. L. Shi, J. W. Liu, X. D. Chen, and J. W. Dong, "Topological Photonic Crystals: Physics, Designs, and Applications," Laser Photonics Rev. **16**, 2100300 (2022).

10. S. Raghu and F. D. M. Haldane, "Analogs of quantum-Hall-effect edge states in photonic crystals," Phys. Rev. A **78**, 033834 (2008).
11. Z. Wang, Y. D. Chong, J. D. Joannopoulos, and M. Soljacic, "Reflection-free one-way edge modes in a gyromagnetic photonic crystal," Phys. Rev. Lett. **100**, 013905 (2008).
12. F. D. Haldane and S. Raghu, "Possible realization of directional optical waveguides in photonic crystals with broken time-reversal symmetry," Phys. Rev. Lett. **100**, 013904 (2008).
13. J. Chen and Z. Y. Li, "Prediction and Observation of Robust One-Way Bulk States in a Gyromagnetic Photonic Crystal," Phys. Rev. Lett. **128**, 257401 (2022).
14. Z. Wang, Y. Chong, J. D. Joannopoulos, and M. Soljacic, "Observation of unidirectional backscattering-immune topological electromagnetic states," Nature **461**, 772-775 (2009).
15. L. H. Wu and X. Hu, "Scheme for Achieving a Topological Photonic Crystal by Using Dielectric Material," Phys. Rev. Lett. **114**, 223901 (2015).
16. T. Ma, A. B. Khanikaev, S. H. Mousavi, and G. Shvets, "Guiding electromagnetic waves around sharp corners: topologically protected photonic transport in metawaveguides," Phys. Rev. Lett. **114**, 127401 (2015).
17. X. Cheng, C. Jouvaud, X. Ni, S. H. Mousavi, A. Z. Genack, and A. B. Khanikaev, "Robust reconfigurable electromagnetic pathways within a photonic topological insulator," Nat. Mater. **15**, 542-548 (2016).
18. Y. Yang, Y. F. Xu, T. Xu, H. X. Wang, J. H. Jiang, X. Hu, and Z. H. Hang, "Visualization of a Unidirectional Electromagnetic Waveguide Using Topological Photonic Crystals Made of Dielectric Materials," Phys. Rev. Lett. **120**, 217401 (2018).
19. M. A. Gorlach, X. Ni, D. A. Smirnova, D. Korobkin, D. Zhirihin, A. P. Slobozhanyuk, P. A. Belov, A. Alu, and A. B. Khanikaev, "Far-field probing of leaky topological states in all-dielectric metasurfaces," Nat. Commun. **9**, 909 (2018).
20. T. Ma and G. Shvets, "All-Si valley-Hall photonic topological insulator," New J. Phys. **18**, 025012 (2016).
21. X. Wu, Y. Meng, J. Tian, Y. Huang, H. Xiang, D. Han, and W. Wen, "Direct observation of valley-polarized topological edge states in designer surface plasmon crystals," Nat. Commun. **8**, 1304 (2017).
22. Y. Kang, X. Ni, X. Cheng, A. B. Khanikaev, and A. Z. Genack, "Pseudo-spin-valley coupled edge states in a photonic topological insulator," Nat. Commun. **9**, 3029 (2018).
23. M. I. Shalaev, W. Walasik, A. Tsukernik, Y. Xu, and N. M. Litchinitser, "Robust topologically protected transport in photonic crystals at telecommunication wavelengths," Nat Nanotechnol **14**, 31-34 (2019).
24. J. W. You, Q. Ma, Z. Lan, Q. Xiao, N. C. Panoiu, and T. J. Cui, "Reprogrammable plasmonic topological insulators with ultrafast control," Nature Communications **12**, 1-7 (2021).
25. J. W. Dong, X. D. Chen, H. Zhu, Y. Wang, and X. Zhang, "Valley photonic crystals for control of spin and topology," Nat. Mater. **16**, 298-302 (2017).
26. Y. Wu, C. Li, X. Hu, Y. Ao, Y. Zhao, and Q. Gong, "Applications of Topological Photonics in Integrated Photonic Devices," Advanced Optical Materials **5**, 1700357 (2017).
27. G. Harari, M. A. Bandres, Y. Lumer, M. C. Rechtsman, Y. D. Chong, M. Khajavikhan, D. N. Christodoulides, and M. Segev, "Topological insulator laser: Theory," Science **359**, eaar4003 (2018).
28. M. A. Bandres, S. Wittek, G. Harari, M. Parto, J. Ren, M. Segev, D. N. Christodoulides, and M. Khajavikhan, "Topological insulator laser: Experiments," Science **359**, eaar4005 (2018).
29. L. Yang, G. Li, X. Gao, and L. Lu, "Topological-cavity surface-emitting laser," Nat. Photonics **16**, 279-283 (2022).
30. Z. Gao, Z. Yang, F. Gao, H. Xue, Y. Yang, J. Dong, and B. Zhang, "Valley surface-wave photonic crystal and its bulk/edge transport," Phys. Rev. B **96**, 201402 (2017).
31. X. T. He, E. T. Liang, J. J. Yuan, H. Y. Qiu, X. D. Chen, F. L. Zhao, and J. W. Dong, "A silicon-on-insulator slab for topological valley transport," Nat. Commun. **10**, 872 (2019).
32. J.-W. Liu, F.-L. Shi, X.-T. He, G.-J. Tang, W.-J. Chen, X.-D. Chen, and J.-W. Dong, "Valley photonic crystals," Advances in Physics: X **6**, 1905546 (2021).
33. F. Gao, H. Xue, Z. Yang, K. Lai, Y. Yu, X. Lin, Y. Chong, G. Shvets, and B. Zhang, "Topologically protected refraction of robust kink states in valley photonic crystals," Nat. Phys. **14**, 140-144 (2017).
34. Y. Yang, Y. Yamagami, X. Yu, P. Pitchappa, J. Webber, B. Zhang, M. Fujita, T. Nagatsuma, and R. Singh, "Terahertz topological photonics for on-chip communication," Nat. Photonics **14**, 446-451 (2020).
35. A. Kumar, Y. J. Tan, N. Navaratna, M. Gupta, P. Pitchappa, and R. Singh, "Slow light topological photonics with counter-propagating waves and its active control on a chip," Nat. Commun. **15**, 926 (2024).
36. R. Jia, S. Kumar, T. C. Tan, A. Kumar, Y. J. Tan, M. Gupta, P. Szriftgiser, A. Alphones, G. Ducournau, and R. Singh, "Valley-conserved topological integrated antenna for 100-Gbps THz 6G wireless," Science Advances **9**, eadi8500 (2023).
37. M. Gupta, A. Kumar, and R. Singh, "Electrically Tunable Topological Notch Filter for THz Integrated Photonics," Advanced Optical Materials **11**, 2301051 (2023).
38. Y. Li, Y. Yu, F. Liu, B. Zhang, and G. Shvets, "Topology-Controlled Photonic Cavity Based on the Near-Conservation of the Valley Degree of Freedom," Phys. Rev. Lett. **125**, 213902 (2020).
39. A. Kumar, M. Gupta, P. Pitchappa, T. C. Tan, U. Chattopadhyay, G. Ducournau, N. Wang, Y. Chong, and R. Singh, "On-Chip Active Control of Ultra-High-Q Terahertz Photonic Topological Cavities," Adv Mater **34**, e2202370 (2022).
40. Y. Chen, X.-T. He, Y.-J. Cheng, H.-Y. Qiu, L.-T. Feng, M. Zhang, D.-X. Dai, G.-C. Guo, J.-W. Dong, and X.-F. Ren, "Topologically Protected Valley-Dependent Quantum Photonic Circuits," Phys. Rev. Lett. **126**, 230503 (2021).
41. H. Wang, L. Sun, Y. He, G. Tang, S. An, Z. Wang, Y. Du, Y. Zhang, L. Yuan, X. He, J. Dong, and Y. Su, "Asymmetric Topological Valley Edge States on Silicon-On-Insulator Platform," Laser Photonics Rev. **16**, 2100631 (2022).
42. J. Ma, C. Ouyang, Y. Yang, H. Li, L. Niu, X. Qian, Y. Liu, B. Yang, Q. Xu, and Y. Li, "Multichannel valley topological beam splitter based on different types of domain walls," Appl. Phys. Lett. **122**, 241701 (2023).
43. F. Zhang, L. He, H. Zhang, L. J. Kong, X. Xu, and X. Zhang, "Experimental Realization of Topologically-Protected All-Optical Logic Gates Based on Silicon Photonic Crystal Slabs," Laser Photonics Rev., 2200329 (2023).
44. Y. Zeng, U. Chattopadhyay, B. Zhu, B. Qiang, J. Li, Y. Jin, L. Li, A. G. Davies, E. H. Linfield, B. Zhang, Y. Chong, and Q. J. Wang, "Electrically pumped topological laser with valley edge modes," Nature **578**, 246-250 (2020).
45. B. Kramer and A. MacKinnon, "Localization: theory and experiment," Rep. Prog. Phys. **56**, 1469 (1993).
46. C. A. Rosiek, G. Arregui, A. Vladimirova, M. Albrechtsen, B. Vosoughi Lahijani, R. E. Christiansen, and S. Stobbe, "Observation of strong backscattering in valley-Hall photonic topological interface modes," Nat. Photonics, 1-7 (2023).
47. K. L. Tsakmakidis, A. D. Boardman, and O. Hess, "'Trapped rainbow' storage of light in metamaterials," Nature **450**, 397-401 (2007).
48. Q. Gan, Y. J. Ding, and F. J. Bartoli, ""Rainbow" trapping and releasing at telecommunication wavelengths," Phys. Rev. Lett. **102**, 056801 (2009).
49. F. Horst, W. M. Green, S. Assefa, S. M. Shank, Y. A. Vlasov, and B. J. Offrein, "Cascaded Mach-Zehnder wavelength filters in silicon photonics for low loss and flat pass-band WDM (de-)multiplexing," Opt Express **21**, 11652-11658 (2013).
50. W. Deng, L. Chen, H. Zhang, S. Wang, Z. Lu, S. Liu, Z. Yang, Z. Wang, S. Yuan, Y. Wang, R. Wang, Y. Yu, X. Wu, X. Yu, and X. Zhang, "On-Chip Polarization- and Frequency-Division Demultiplexing for Multidimensional Terahertz Communication," Laser Photonics Rev. **16**, 2200136 (2022).

51. H. Hu, D. Ji, X. Zeng, K. Liu, and Q. Gan, "Rainbow trapping in hyperbolic metamaterial waveguide," Scientific reports **3**, 1249 (2013).
52. L. Zhang, M. Z. Chen, W. Tang, J. Y. Dai, L. Miao, X. Y. Zhou, S. Jin, Q. Cheng, and T. J. Cui, "A wireless communication scheme based on space-and frequency-division multiplexing using digital metasurfaces," Nature electronics **4**, 218-227 (2021).
53. K. L. Tsakmakidis, T. W. Pickering, J. M. Hamm, A. F. Page, and O. Hess, "Completely stopped and dispersionless light in plasmonic waveguides," Phys. Rev. Lett. **112**, 167401 (2014).
54. J. Li, G. Hu, L. Shi, N. He, D. Li, Q. Shang, Q. Zhang, H. Fu, L. Zhou, W. Xiong, J. Guan, J. Wang, S. He, and L. Chen, "Full-color enhanced second harmonic generation using rainbow trapping in ultrathin hyperbolic metamaterials," Nat. Commun. **12**, 6425 (2021).
55. T. Niemi, L. H. Frandsen, K. K. Hede, A. Harpoth, P. I. Borel, and M. Kristensen, "Wavelength-division demultiplexing using photonic crystal waveguides," IEEE Photonics Technology Letters **18**, 226-228 (2006).
56. C. Lu, C. Wang, M. Xiao, Z. Q. Zhang, and C. T. Chan, "Topological Rainbow Concentrator Based on Synthetic Dimension," Phys. Rev. Lett. **126**, 113902 (2021).
57. S. Elshahat, C. Wang, H. Zhang, and C. Lu, "Perspective on the topological rainbow," Appl. Phys. Lett. **119**, 230505 (2021).
58. Y. Mao, Z. Li, W. Hu, X. Dai, and Y. Xiang, "Topological slow light rainbow trapping and releasing based on gradient valley photonic crystal," J. Lightwave Technol., 5152-5156 (2022).
59. C. Lu, Y. Z. Sun, C. Wang, H. Zhang, W. Zhao, X. Hu, M. Xiao, W. Ding, Y. C. Liu, and C. T. Chan, "On-chip nanophotonic topological rainbow," Nat. Commun. **13**, 2586 (2022).
60. X. Wang, W. Zhao, S. Elshahat, and C. Lu, "Topological rainbow trapping based on gradual valley photonic crystals," Frontiers in Physics **11**, 1141997 (2023).
61. Z. Qi, G. Hu, C. Deng, H. Sun, Y. Sun, Y. Li, B. Liu, Y. Bai, S. Chen, and Y. Cui, "Electrical tunable topological valley photonic crystals for on-chip optical communications in the telecom band," Nanophotonics **11**, 4273-4285 (2022).
62. A. Kumar, M. Gupta, P. Pitchappa, N. Wang, P. Szriftgiser, G. Ducournau, and R. Singh, "Phototunable chip-scale topological photonics: 160 Gbps waveguide and demultiplexer for THz 6G communication," Nature Communications **13**, 5404 (2022).
63. Y. Ruan, X. Qian, H.-X. Wang, Z.-D. Hu, Y. Yang, J. Wang, X. Shen, and Y. Wang, "Applications for wavelength division multiplexers based on topological photonic crystals," Photonics Res. **11**, 569-574 (2023).
64. G.-J. Tang, X.-D. Chen, F.-L. Shi, J.-W. Liu, M. Chen, and J.-W. Dong, "Frequency range dependent topological phases and photonic detouring in valley photonic crystals," Phys. Rev. B **102**, 174202 (2020).
65. F. Gao, Z. Gao, X. Shi, Z. Yang, X. Lin, H. Xu, J. D. Joannopoulos, M. Soljacic, H. Chen, L. Lu, Y. Chong, and B. Zhang, "Probing topological protection using a designer surface plasmon structure," Nat. Commun. **7**, 11619 (2016).
66. J. Pendry, L. Martin-Moreno, and F. Garcia-Vidal, "Mimicking surface plasmons with structured surfaces," Science **305**, 847-848 (2004).
67. X.-D. Chen, F.-L. Shi, H. Liu, J.-C. Lu, W.-M. Deng, J.-Y. Dai, Q. Cheng, and J.-W. Dong, "Tunable Electromagnetic Flow Control in Valley Photonic Crystal Waveguides," Phys. Rev. Appl. **10**, 044002 (2018).